SURFACE CHEMISTRY

Real-space investigations of on-surface intermolecular radical transfer reactions assisted by persistent radicals

Huaming Zhu[1]†, Junbo Wang[1,2]†, Kaifeng Niu[3]†, Yong Zhang[4]†, Yi Zhang[4], Chuan Deng[1], Peipei Huang[1], Dengyuan Li[5], Peinian Liu[5], Jianchen Lu[4], Johanna Rosen[3], Jonas Björk[3]*, Jinming Cai[4]*, Lifeng Chi[2]*, Qing Li[1]*

Synthesizing radicals that have both long lifetimes and high chemical reactivity remains a long-term challenge. Here, persistent phenyl radicals are successfully synthesized on Ag(111) by protecting the carbon radical site by designing the precursor molecule with suitable steric hindrance. As carbon-carbon coupling is prohibited, such radicals remain intact for longer than 6 hours at room temperature on Ag(111). Taking advantage of the long lifetimes, the as-synthesized radicals are directly characterized in the real space at the single-chemical-bond scale by means of bond-resolving scanning tunneling microscopy imaging. Accompanied by the excellent stability, the radicals exhibit high chemical reactivities and facilitate the intermolecular radical transfer reactions at extreme low temperature. The preparation of persistent radicals not only favors the characterization of a surface-stabilized radical in the real space but also aids in illuminating the detailed reaction pathways of subsequent radical-assisted reactions directly.

INTRODUCTION

Free radicals are single-electron species created through the homolysis of covalent bonds (1). The presence of singly occupied molecular orbitals makes most radicals extremely reactive. Consequently, radicals usually have very short lifetimes and facilitate a broad range of hydrogen abstraction, dimerization, recombination, and polymerization reactions (2–4). The short lifetimes of reactive radicals make them difficult to characterize in the real space. Conventionally, the processes of radical reactions are studied indirectly by electron spin resonance spectroscopy (5). On the other hand, few radicals have very long lifetimes and survive almost indefinitely, which are known as persistent radicals (6). Persistent radicals mostly arise from electronic stabilization, and the single electron of the persistent radical is usually carried by an oxygen or nitrogen atom (7, 8). Nevertheless, the long lifetimes of persistent radicals reduce their access to radical-related reactivity. A trade-off between the reactivity and the stability of radicals is therefore often required. The demand for investigating reactive radicals in the real space and obtaining direct evidence of radical transfer reactions necessitates the development of methodologies to synthesize radicals that simultaneously have long lifetimes and high chemical reactivity.

On-surface synthesis provides alternatives for the real-space recognition of monomers and oligomers at the single-molecule scale (9–19). Within this domain, diverse low-dimensional functional nanostructures with atomic precision have been successfully constructed on various substrates (20–35). Specifically, on-surface synthesis has the following advantages: (i) Reaction precursors and products can be characterized in situ in the real space at the subatomic level with the aid of advanced imaging techniques (36–40). (ii) Because of the absence of contaminations in the ultrahigh vacuum chamber, on-surface chemistry provides ideal model systems for exploring reaction pathways (41–44). (iii) Intermediate states elusive in solution reactions may be traced on surfaces once they are stabilized via considerable substrate-molecule interactions (45–47). Despite extensive studies, characterizing reactive radicals in the real space remains challenging (48). Taking the Ullmann-like reaction of aryl halides as an example, as the generated phenyl radicals are extremely reactive, they are imaged by scanning tunneling microscopy (STM) only after being passivated by H atoms, metal adatoms, or other phenyl radicals (49).

Recently, our group reported intermolecular radical transfer reactions on metal surfaces (50). The strong electron-withdrawing phenyl radicals, generated from homolysis of Ph-X bonds (X = Br and I), facilitate subsequent C—H activations of alkynyl and amino groups with high yields. However, two major questions remain: (i) The phenyl radical intermediates cannot be monitored in the real space because radical transfer reactions take place as soon as phenyl radicals are generated. Therefore, the radical transfer mechanism is proposed by various indirect evidence (calculated pathways, stoichiometric analysis, etc.). (ii) The reaction required relative higher temperatures because the radical generation is the limiting step. It is therefore necessary to decouple the radical generation and transfer processes by creating persistent phenyl radicals on metal surfaces.

Herein, persistent phenyl radicals are successfully synthesized on Ag(111) via the introduction of steric hindrance in precursor molecules [2-iodo-1,3-diphenylbenzene (ITP)]. As C—C coupling following an initial dehalogenation is prohibited, such radicals remain intact for longer than 6 hours at room temperature (RT), and only 0.48% of the radicals are passivated by residual hydrogen in the vacuum chamber after annealing the surface at 370 K for 20 min. By systematical experiments and density functional theory (DFT) calculations, the passivation barrier is calculated to be 0.84 eV. Taking advantage of the long lifetime, both the as-synthesized radicals and H-passivated radicals can be directly investigated in the real

[1]School of Physics and Information Technology, Shaanxi Normal University, Xi'an 710119, China. [2]Institute of Functional Nano & Soft Materials (FUNSOM), Jiangsu Key Laboratory for Carbon-Based Functional Materials & Devices, Soochow University, Suzhou 215123, China. [3]Department of Physics, Chemistry and Biology, IFM, Linköping University, Linköping 58183, Sweden. [4]Faculty of Materials Science and Engineering, Kunming University of Science and Technology, Kunming 650093, China. [5]State Key Laboratory of Natural Medicines, Department of Medicinal Chemistry, China Pharmaceutical University, Nanjing 211198, P. R. China.
*Corresponding author. Email: jonas.bjork@liu.se (J.B.); j.cai@kust.edu.cn (J.C.); chilf@suda.edu.cn (L.C.); liqing@snnu.edu.cn (Q.L.)
†These authors contributed equally to this work.

space at the single-chemical-bond scale by means of STM and bond-resolving STM (BR-STM) imaging. Accompanied by the excellent stability, the radicals exhibit high chemical reactivities. With the participation of the as-synthesized phenyl radicals, the dehydrogenation of the terminal alkynes of a coadsorbed molecule takes place at temperatures as low as 200 K on Ag(111), in stark contrast to the nondehydrogenated coupling of the same molecule taking place at 400 K on the same surface without the assistance of radicals. Moreover, as by-products via Ullmann alternative reaction pathways are excluded, the reaction equation can be accurately deduced such that the distribution of reaction products is precisely controlled by the rational choice of stoichiometric ratios of precursor molecules. In conclusion, we have synthesized radicals that simultaneously have long lifetimes and high chemical reactivity via the introduction of steric hindrance. The decoupling of the radical generation and subsequent reaction processes not only favors the characterization of a single free radical in the real space and provides direct and undoubted evidence for the on-surface radical transfer mechanism but also lowers the reaction temperature. Moreover, the metal surface functionalized with persistent radicals provides an artificial active template, allowing for a broad range of on-surface reactions.

RESULTS AND DISCUSSION
Preparation and characterization of persistent radicals on Ag(111)

Figure 1A gives a representative STM image after depositing 0.3–monolayer (ML) ITP (the structural model is illustrated in the inset) on a Ag(111) surface held at RT. Two kinds of distinct objects are observed: One manifests as an isolated ring, and the other is a V-shaped monomer (complex **I**) that self-assembles into small islands. As iodine atoms are known to detach from iodobenzene on Ag(111) below RT (51, 52), bright spots within the islands can be attributed to detached iodine adatoms. The isolated ring is stabilized after cooling the sample to 4.2 K (Fig. 1B) and exhibits the same morphology as that of complex **I**. Moreover, by artificially removing the complex **I** monomer from the periphery of the island to the terrace at 77 K, such a monomer transforms to the isolated ring (Fig. 1, C and D). The cooling and tip manipulation experiments indicate that both the isolated ring and complex **I** can be ascribed to dehalogenated ITP (deI-ITP). The isolated deI-ITP molecule rotates around the surface atom to which it is chemically attached, and the rotation can be hindered either by self-assembly into islands or cooling to lower temperatures (the detailed rotation mechanism can be found in fig. S1).

The structure shown in Fig. 1A, interpreted as a surface-stabilized radical, remains unaltered after annealing the surface at RT for more than 6 hours (fig. S2). Distinct structural evolution takes place after annealing the sample at 370 K for 20 min (Fig. 2). In addition to the dominating ring structures and complex **I** objects, few new products are formed (complex **II**), as highlighted by the arrows in Fig. 2A (77 K) and Fig. 2B (4.2 K). To elucidate the nature of complex **II**, high-resolution STM and BR-STM investigations and corresponding DFT optimizations are carried out. The dehalogenated benzene ring of complex **I** is exhibited as a bright protrusion in the STM image (Fig. 2C) and a depressed shadow in the BR-STM image (Fig. 2D and fig. S3),
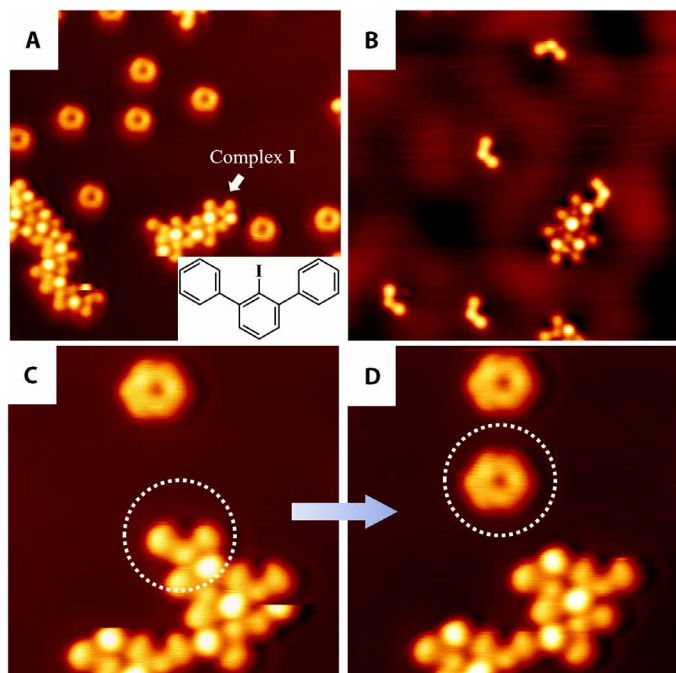

Fig. 1. Adsorption of ITP on Ag(111). (**A**) STM image after depositing 0.3-ML ITPs onto Ag(111) held at RT. (**B**) STM image acquired after cooling the surface shown in (A) to 4.2 K. (**C** and **D**) Tip manipulation experiment by artificially removing a monomer from the periphery of the island. Scanning parameters: (A) $I_t = 20$ pA, $V_b = -1$ V; (B) $I_t = 50$ pA, $V_b = 500$ mV, $T = 4.2$ K; [(C) and (D)] $I_t = 20$ pA, $V_b = -1$ V. The image sizes are 20 nm by 20 nm for [(A) and (B)] and 5 nm by 5 nm for [(C) and (D)].
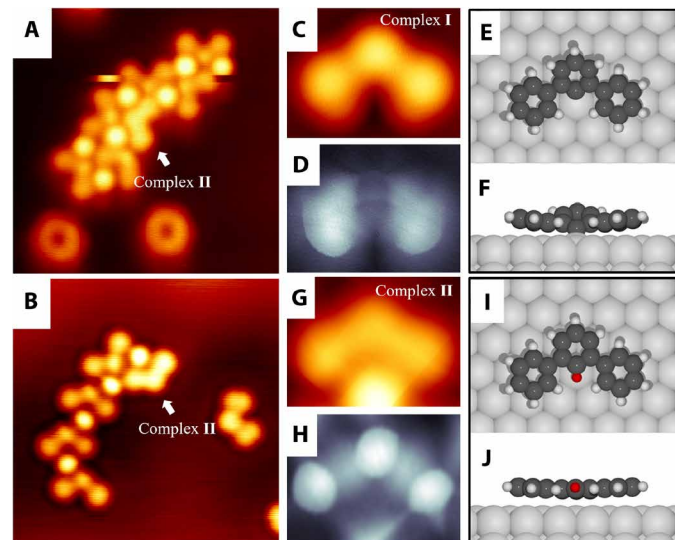

Fig. 2. Passivation of phenyl radicals. (**A**) STM image after annealing the sample shown in Fig. 1A at 370 K for 20 min. (**B**) STM image after cooling the sample shown in (A) to 4.2 K. (**C** and **D**) High-resolution STM topographic and BR-STM images of complex **I**. (**E** and **F**) Top and side views of the DFT-optimized structural model of complex **I**. (**G** and **H**) High-resolution STM topographic and BR-STM images of complex **II**. (**I** and **J**) Top and side views of the DFT-optimized structural model of complex **II**. The Ag, C, and H atoms are represented by the silver, gray, and white atoms, respectively. The H atom that passivates complex **I** was highlighted in red. Scanning parameters: (A) $I_t = 20$ pA, $V_b = -1$ V; [(B), (C), and (G)] $I_t = 50$ pA, $V_b = 500$ mV, $T = 4.2$ K; [(D) and (H)] $I_t = 50$ pA, $V_b = 2$ mV, $T = 4.2$ K. The image sizes are 10 nm by 10 nm for [(A) and (B)] and 1.2 nm by 1 nm for [(C), (D), (G), and (H)].

which can be ascribed to the tilting of the dehalogenated benzene ring induced by the interaction between the phenyl radical of complex **I** and the Ag(111) surface (Fig. 2, E and F). Complex **II**, however, exhibits smooth density of states in the STM topographic image (Fig. 2G and fig. S4), and three benzene rings of complex **II** show identical configurations in the BR-STM image (Fig. 2H and fig. S3). We therefore attribute complex **II** to H-passivated deI-ITPs. The corresponding optimized structure of complex **II** is illustrated in Fig. 2 (I and J), in which the H-passivated monomer adsorbs on Ag(111) with a planar configuration, consistent with the STM and BR-STM investigations. Note that because of the weak interaction between the H-passivated monomer and the silver substrate, complex **II** can only be observed in the self-assembled islands.

Conventionally, Ullmann couplings of iodobenzene precursors take place below RT on Ag(111) (*51, 52*). However, because of the presence of steric hindrance, phenyl radicals of deI-ITP remain intact until they have been passivated by residual hydrogen atoms in the vacuum chamber (Fig. 2). To analyze the stability of phenyl radicals quantitatively, delicate annealing experiments are performed (see fig. S5 for details). The H-passivation yields are 0, 0.48, 4.83, and 9.86% after annealing at RT, 370 K, 400 K, and 420 K, respectively, for 20 min (Fig. 3A). According to the Arrhenius equation, the H-passivation yields and annealing temperatures have the following relation

$$\ln(p) = -\frac{E_a}{RT} + C$$

where p is the H-passivation yield, E_a is the activation energy for H-passivation of phenyl radicals of ITP, R is the gas constant, T is the temperature, and C is a constant (see the Supplementary Materials for details). An excellent linear fit is obtained (Fig. 3B), with an activation energy of 0.82 ± 0.1 eV. The H-passivation barrier is further evaluated by DFT calculations. We consider both an adsorbed H atom and H_2 molecules as the source of hydrogen, and the corresponding passivation barriers are 0.84 eV (Fig. 3C) and 0.94 eV (fig. S6), respectively, both close to the empirically deduced value.

In short conclusion, by introducing steric hindrance in iodobenzene precursors, we successfully prepared persistent phenyl radicals on a Ag(111) surface. The persistent radicals remain intact for longer than 6 hours at RT, and only 0.48% of the radicals are passivated by residual protons in the vacuum chamber after annealing the surface at 370 K for 20 min by overcoming an activation energy of 0.84 eV. Taking advantage of the long lifetime, the thermally triggered abundant free radicals are successfully characterized at the single-chemical-bond scale in the real space by means of STM and BR-STM imaging. Last, we note that such a steric hindrance strategy is rather universal for synthesizing persistent radicals on metal surfaces (see fig. S7 for details).

Chemical activity of persistent radicals on Ag(111)

To investigate the reactivity of as-synthesized persistent surface-stabilized radicals, an additional molecule [1,3,5-tris-(4-ethynylphenyl) benzene (Ext-TEB)], which exhibits threefold symmetry and is functionalized with terminal alkynes, is introduced. The radicals/Ag(111) surface is initially prepared by depositing 0.3-ML ITP molecules on Ag(111) held at RT, on which all iodine atoms are detached (see fig. S8 for details). Diverse self-assembly islands are observed after subsequently depositing 0.1-ML Ext-TEB (the ratio between the number of phenyl radicals and
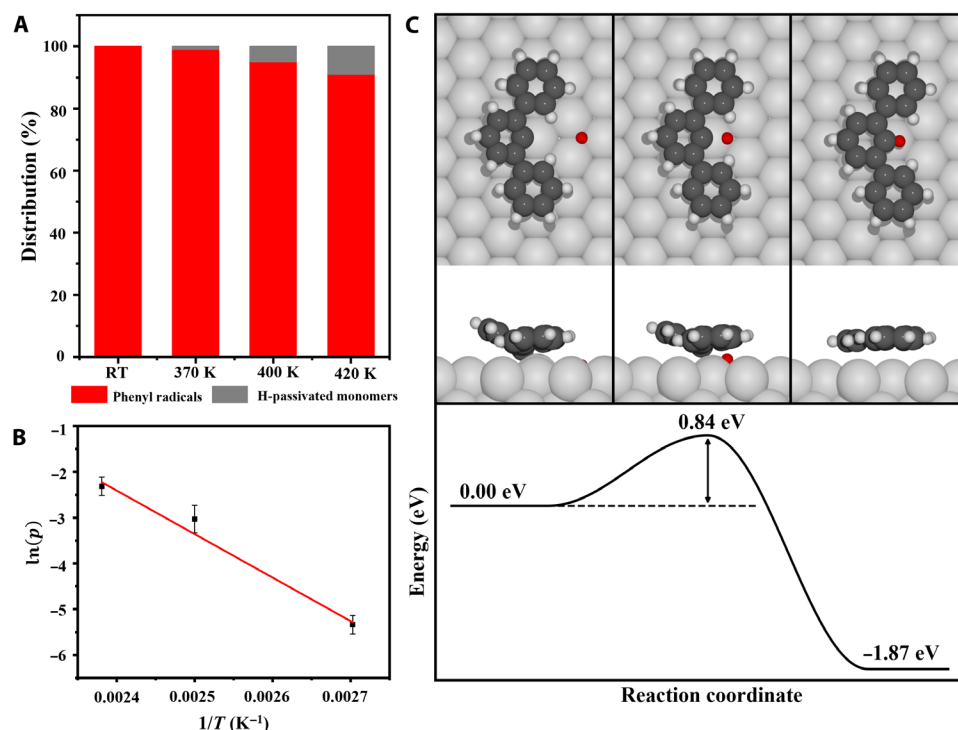

Fig. 3. Analysis of the H-passivation process. (**A**) Distribution of products after annealing the ITP/Ag(111) sample at different annealing temperatures for 20 min. (**B**) Relation between $\ln(p)$ and $1/T$ according to eq. S10. (**C**) Reaction pathway and the corresponding energy profile of the passivation of a phenyl radical by a hydrogen atom. The Ag, C, and H atoms are represented by the silver, gray, and white atoms, respectively. The H atom that passivates complex **I** was highlighted in red.

alkynyl groups r is therefore close to 1) onto a cold radicals/Ag(111) surface held at 200 K, as shown in Fig. 4 (A and B). ITP precursors exhibit two configurations: (i) isolated rings (Fig. 4C), which is the same as that shown in Fig. 1A (deI-ITPs); (ii) close-packed islands (Fig. 4D), which can be ascribed to the self-assembly of complex **II** (H-passivated ITP; see fig. S9 for details). Similarly, two kinds of islands are observed for Ext-TEB precursors, and they can be ascribed to the self-assembly of dehydrogenated (Fig. 4E) (*53*) and intact Ext-TEB (Fig. 4F) precursors (see fig. S10 for details).

Statistical analysis (Fig. 4G) discloses that 82% of phenyl radicals of deI-ITP are passivated and 18% of them remain intact, which differs from the fact that isolated phenyl radicals of deI-ITP remain unaltered at RT for longer than 6 hours. Meanwhile, 81% of terminal alkynes of Ext-TEB have hydrogen atoms detached, and 19% of them remain intact. The observed phenomena are in excellent agreement with our recently proposed intermolecular radical transfer mechanism (Fig. 4H) (*50*). Calculated reaction barriers for the direct dehydrogenation of terminal alkynes with and without the assistance of phenyl radicals are 0.78 eV (*50*) and 1.82 eV (*54*), respectively, naturally explaining why 81% of deprotonation reaction of alkynyl groups takes place at a cold Ag(111) surface (200 K) in the presence of surface-stabilized radicals. In sharp contrast, in the absence of radicals, direct dehydrogenation of the precursor does not take place and, instead, the Ext-TEB molecules couple at 400 K (*55*, *56*) on Ag(111) by forming an enyne bonding motif (fig. S11) (*56–59*). It should be noted that the enyne formation follows an overall lower energy landscape than the direct dehydrogenation but higher than the radical-assisted dehydrogenation. The intermolecular radical transfer reaction is accomplished via the hydrogen migration from alkynyl groups to phenyl radicals, leading to the finding that the dehydrogenation reaction of Ext-TEB and the H-passivation reaction of deI-ITP

take place simultaneously (*50*, *60*). Mechanistically, one phenyl radical can only trigger the dehydrogenation of one alkyne group (Fig. 4H), which is in excellent consistence with the fact that the passivation yield of phenyl radicals (82%) is close to the dehydrogenation yield of alkyne groups (81%) at this stage on Ag(111). Moreover, it should be noted that deI-ITPs are free to move on Ag(111) when the radical transfer reaction takes place (see fig. S12 for details), although they are stabilized on the surface at 77 K. Therefore, it is the free radicals (not surface-stabilized radicals) that lead to the radical transfer reactions.

A complete radical transfer reaction is achieved upon slightly annealing the sample to 250 K. All Ext-TEB precursors self-assemble into porous networks (Fig. 5A), decorated by trapped ITP molecules. The highly resolved STM image (Fig. 5B) discloses that adjacent Ext-TEB monomers are linked by a bright protrusion, indicating the formation of alkynyl-Ag-alkynyl motifs. We therefore obtained the structural model of the networks (Fig. 5C), and the measured pore-to-pore distance (3.58 ± 0.10 nm) is in excellent agreement with previous reports (*50*, *53*). Accompanied by the formation of porous networks, close-packed islands are observed on the Ag(111) surface (Fig. 5, D and E), which is composed of H-passivated ITP precursors and detached iodine adatoms. In summary, we successfully synthesized phenyl radicals on a Ag(111) surface that simultaneously have two competing characteristics: high stability and high reactivity. The synthesized radicals facilitate the subsequent intermolecular radical transfer reaction with yields of 81% at 200 K and 100% at 250 K on Ag(111).

As Ullmann coupling side reactions are prohibited, the introduction of steric hindrance facilitates us to tune the reaction products in a fine-controlled manner. We examined the reaction products at RT by rationally adjusting the stoichiometric ratio of precursor molecules. The representative STM images are shown in Fig. 6 and
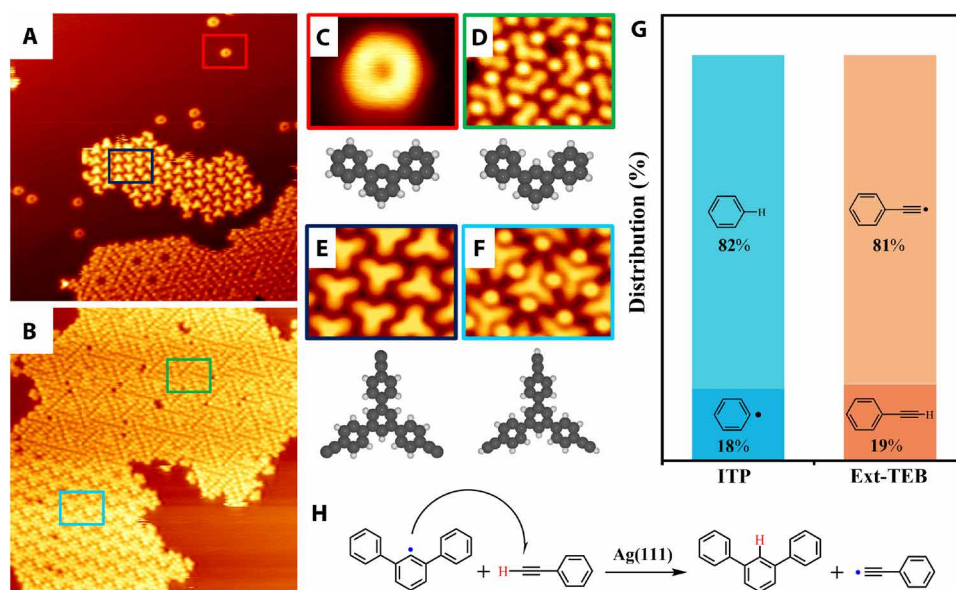

Fig. 4. Reactivity of ITP radicals at 200 K. (**A** and **B**) STM images after depositing 0.1-ML Ext-TEB onto ITP/Ag(111) held at 200 K ($r \approx 1$). The samples are subsequently annealed at 200 K for 20 min. (**C** to **F**) High-resolution STM images and corresponding structural models (lower panels) of (A) and (B). (**G**) Distribution of reaction products. (**H**) Schematic illustration of the intermolecular radical transfer reaction. Tunneling parameters are $I_t = 20$ pA and $V_b = -1$ V for all STM images. The image sizes are 30 nm by 30 nm for [(A) and (B)] and 3 nm by 2 nm for [(C) to (F)].
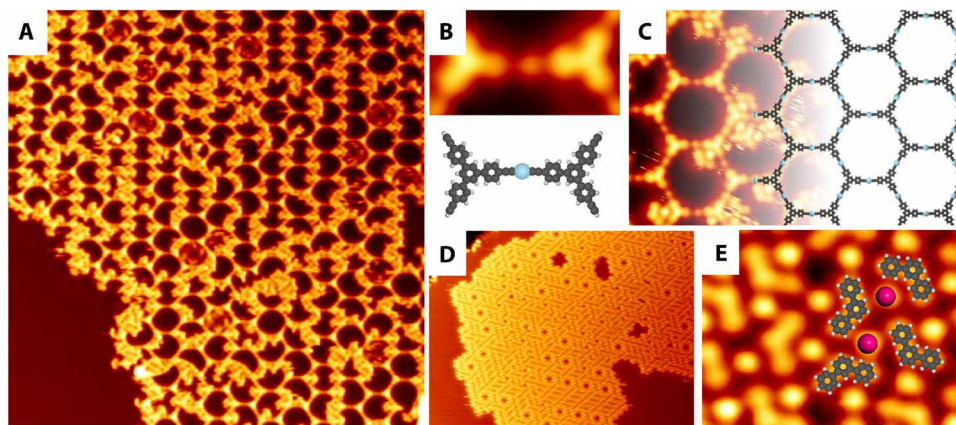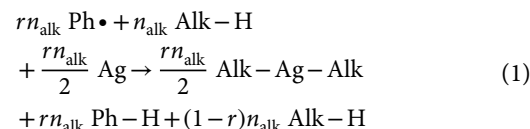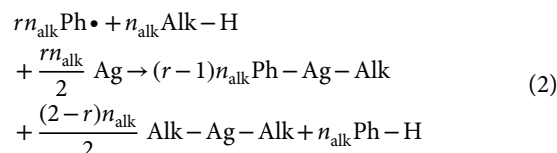
Fig. 5. Reactivity of ITP radicals at 250 K. (**A**) Large-scale STM image of Ext-TEB islands after annealing the sample shown in Fig. 4 ($r \approx 1$) to 250 K for 20 min. (**B**) High-resolution STM image and the corresponding structural model (lower panel) of a linkage unit. (**C**) High-resolution STM image of (A) overlaid with the corresponding structure model. (**D**) Large-scale STM image of ITP islands after annealing the sample shown in Fig. 4 to 250 K. (**E**) High-resolution STM image of (D) overlaid with the corresponding structure model. Tunneling parameters are $I_t = 20$ pA and $V_b = -1$ V for all STM images. The image sizes are 50 nm by 50 nm for (A), 4 nm by 2 nm for (B), 10 nm by 6 nm for (C), 30 nm by 18 nm for (D), and 5 nm by 3 nm for (E).

fig. S13. With the absence of phenyl radicals ($r = 0$), Ext-TEB remains intact at RT and self-assembles into close-packed islands on Ag(111) (Fig. 6A) (*55*). Alkynyl radicals are generated through the radical transfer mechanism at increased r, because it only needs to overcome a moderate energy barrier of 0.78 eV (*50*). Experimentally, most Ext-TEBs transform to dimer products formed by alkyne-Ag-alkyne interactions at $r \approx 0.3$, indicating partial dehydrogenation of the terminal alkynl groups (Fig. 6B). Accompanied by this, H-passivated deI-ITP and intact Ext-TEB self-assemble into different islands on the surface (fig. S14). At an increased r ($r \approx 0.6$, Fig. 6C), more hydrogen atoms detached from alkynyl groups, and regular porous networks are eventually synthesized at $r \approx 1$ (Fig. 6D). The porous networks gradually collapse at further increased r and transform to phenyl-Ag-alkynyl motifs ($r \approx 1.3$ in Fig. 6E and $r \approx 1.6$ in Fig. 6F). At $r \approx 2$, the porous networks transform to the self-assembly islands shown in Fig. 6G, in which the phenyl-Ag-alkynyl bonds dominate. At $r \leq 2$, phenyl radicals either are passivated by hydrogen atoms or form a phenyl-Ag-alkynyl bond. At $r > 2$, however, residual phenyl radicals are observed to adsorb on the surface (highlighted by the arrows in Fig. 6H), which again evidenced the stability of the prepared radicals.
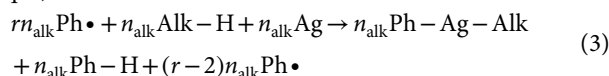
The experimentally observed stoichiometric ratio-dependent reaction pathways can be well explained by the radical transfer mechanism. For convenience, we define the number of phenyl radicals as n_{rad} and the number of alkyne groups as n_{alk}. As shown by experimental results, pathways can be categorized into two scenarios, in which all phenyl radicals will be passivated by alkyne groups if $n_{rad} < n_{alk}$, while phenyl radicals will form organometallic structures or remain as surface-stabilized radicals if $n_{rad} > n_{alk}$. Detailed reactions can be quantitatively written by considering the ratio between n_{rad} and n_{alk}, $r = \frac{n_{rad}}{n_{alk}}$. When $0 < r \leq 1$, only rn_{alk} alkyne groups are activated with the assistance of rn_{alk} phenyl radicals via the radical transfer mechanism, resulting in the formation of $\frac{rn_{alk}}{2}$ alkynyl-Ag-alkynyl linkages. Meanwhile, all rn_{alk} phenyl radicals are passivated by H atoms that migrated from alkyne groups, while the remaining $(1-r)n_{alk}$ alkyne groups remain intact, as shown in Eq. 1

$$rn_{alk}\,Ph\bullet + n_{alk}\,Alk-H$$
$$+ \frac{rn_{alk}}{2}\,Ag \rightarrow \frac{rn_{alk}}{2}\,Alk-Ag-Alk \quad (1)$$
$$+ rn_{alk}\,Ph-H + (1-r)n_{alk}\,Alk-H$$

The corresponding activation yield of alkynes is $r \times 100\%$, which naturally explains why partial ($r \approx 0.3, 0.6$) and all alkyne groups ($r \approx 1$) are activated, respectively (Fig. 6, B to D). When $1 < r \leq 2$, n_{alk} phenyl radicals are passivated via the radical transfer mechanism, and all (n_{alk}) alkyne groups are activated. The remaining $(r-1)n_{alk}$ phenyl radicals interact with dehydrogenated alkyne groups by forming $(r-1)n_{alk}$ phenyl-Ag-alkynyl moieties. Other dehydrogenated alkyne groups form $\frac{(2-r)n_{alk}}{2}$ alkynyl-Ag-alkynyl moieties (Eq. 2)

$$rn_{alk}Ph\bullet + n_{alk}Alk-H$$
$$+ \frac{rn_{alk}}{2}\,Ag \rightarrow (r-1)n_{alk}Ph-Ag-Alk \quad (2)$$
$$+ \frac{(2-r)n_{alk}}{2}\,Alk-Ag-Alk + n_{alk}Ph-H$$

in agreement with the evolution from porous networks at $r \approx 1$ (Fig. 6D) to phenyl-Ag-alkynyl moieties at $r \approx 1.3, 1.6$, and 2 (Fig. 6, E to G). At $r > 2$, n_{alk} phenyl radicals are passivated via the radical transfer mechanism, which is same to that at $1 < r \leq 2$. However, only n_{alk} of the remaining $(r-1)n_{alk}$ phenyl radicals interact with dehydrogenated alkyne groups by forming n_{alk} phenyl-Ag-alkynyl moieties (Eq. 3)

$$rn_{alk}Ph\bullet + n_{alk}Alk-H + n_{alk}Ag \rightarrow n_{alk}Ph-Ag-Alk$$
$$+ n_{alk}Ph-H + (r-2)n_{alk}Ph\bullet \quad (3)$$

As phenyl radicals are in excess, residual $(r-2)n_{alk}$ phenyl radicals anchor on the surface separately (Fig. 6H).

On the basis of Eqs. 1 to 3, we obtained the distribution of different products of alkynyl and phenyl groups with different values of r, as depicted in Table 1. The corresponding theoretical curves are exhibited in Fig. 6 (I and J), which are in excellent agreement with the experimental observations (dots in Fig. 6, I and J). The correlation
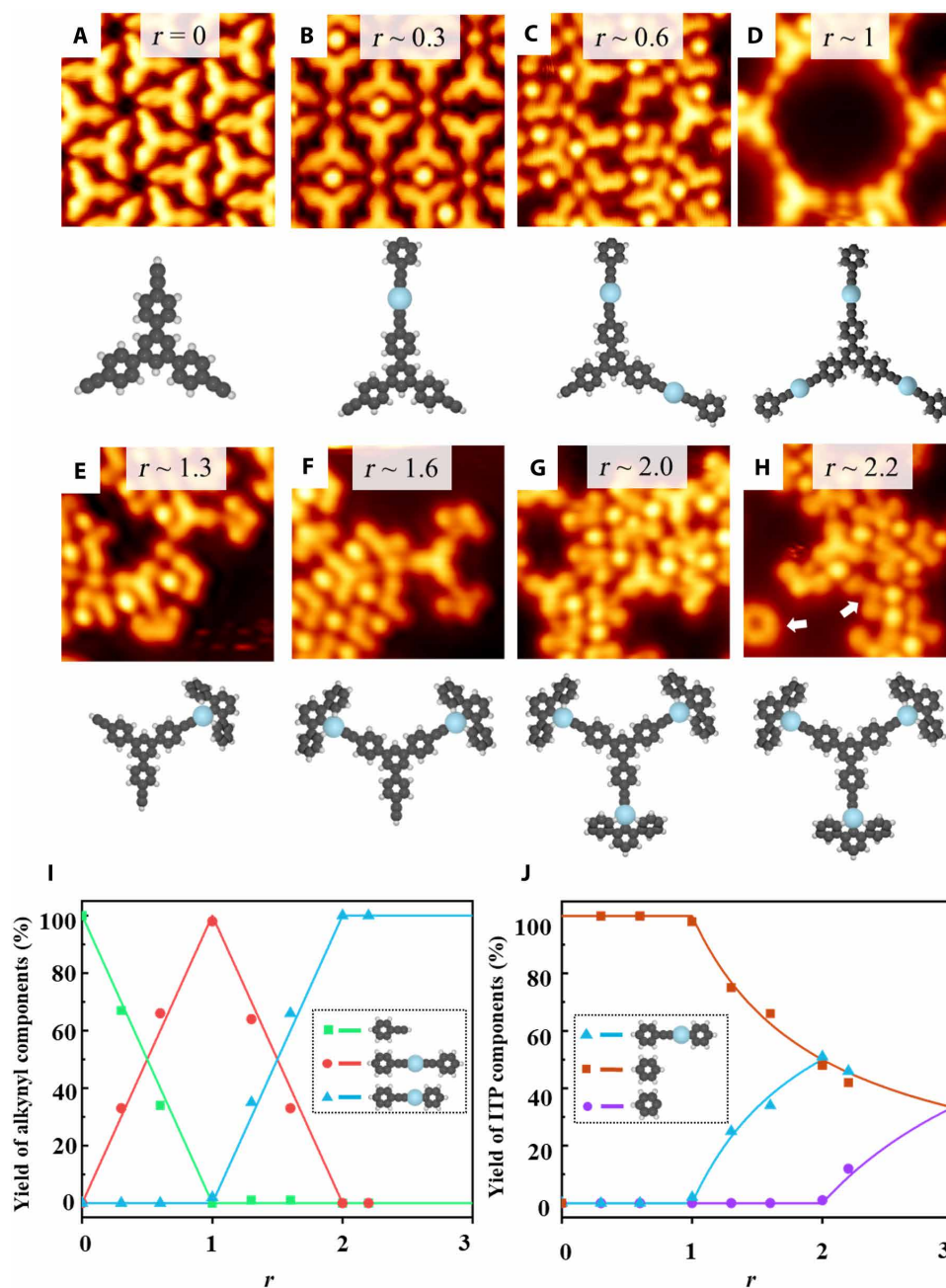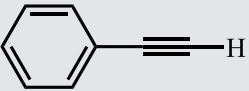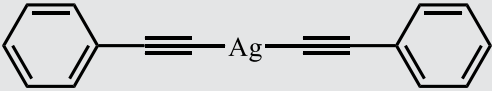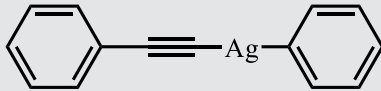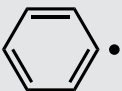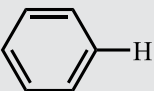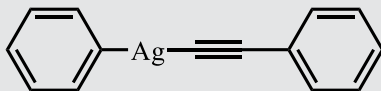
Fig. 6. Distribution of products. Representative STM images and corresponding structure models (lower panels) by codepositing Ext-TEB and ITP on Ag(111) held at RT with (**A**) $r = 0$, (**B**) $r \approx 0.3$, (**C**) $r \approx 0.6$, (**D**) $r \approx 1$, (**E**) $r \approx 1.3$, (**F**) $r \approx 1.6$, (**G**) $r \approx 2.0$, and (**H**) $r \approx 2.2$. The samples are subsequently annealed at RT for 20 min. (**I**) Calculated and experimental yields of alkynyl components as a function of r. (**J**) Calculated and experimental yields of ITP components as a function of r. Tunneling parameters are $I_t = 20$ pA and $V_b = -1$ V for all STM images. The image sizes are 5 nm by 5 nm for all STM images. The Ag, C, and H atoms are represented by the blue, gray, and white circles, respectively.

between the experimental investigation and proposed equations not only further convinces the occurrence of the intermolecular radical transfer reactions but also demonstrates that reaction products can be accurately controlled by inhibiting the Ullmann side reactions.

It is also worthy to point out that Eqs. 1 to 3 are deduced on the basis of an ideal thermodynamic equilibrium analysis, which implies that the saturation of phenyl radicals has top priority. In other words, the passivation by migrated hydrogen atoms is before the formation of phenyl-Ag-alkynyl moieties for phenyl radicals, while

the formation of phenyl-Ag-alkynyl moieties is before the formation of alkynyl-Ag-alkynyl linkages for alkynyl groups. Such a hypothesis is supported by a previous report that the formation of alkynyl-Ag-alkynyl linkages is reversible on Ag(111) (*61*). To further confirm the reversibility of alkynyl-Ag-alkynyl linkages, control experiments are carried out. Different from experiments shown in Fig. 6 that each phase with variable r is synthesized by depositing Ext-TEB on a fresh radicals/Ag(111) surface, we continuously deposit extra ITPs onto the previously characterized Ext-TEBs + ITPs/Ag(111) surface

Table 1. Distribution of alkynyl and phenyl groups with r variables.

Distribution of alkynyl groups of Ext-TEB			
r	(phenyl–C≡C–H)	(phenyl–C≡C–Ag–C≡C–phenyl)	(phenyl–C≡C–Ag–phenyl)
$0 < r \leq 1$	$(1-r) \times 100\%$	$r \times 100\%$	0
$1 < r \leq 2$	0	$(2-r) \times 100\%$	$(r-1) \times 100\%$
$r > 2$	0	0	100%

Distribution of phenyl groups of ITP			
r	(phenyl radical)	(phenyl–H)	(phenyl–Ag–C≡C–phenyl)
$0 < r \leq 1$	0	100%	0
$1 < r \leq 2$	0	$1/r \times 100\%$	$(r-1)/r \times 100\%$
$r > 2$	$(r-2)/r \times 100\%$	$1/r \times 100\%$	$1/r \times 100\%$

in this series of control experiments. With increased values of r, the status of alkynyl components gradually evolve from dimer products to porous networks and, eventually, phenyl-Ag-alkynyl moieties are formed (see fig. S15 for details). The control experiments undoubtedly disclose that the reaction pathways of this codeposition system are thermodynamically driven so that the deduced Eqs. 1 to 3 are conceivable.

To conclude, we successfully synthesized surface-stabilized radicals with both long lifetimes and high chemical reactivity on Ag(111). Such persistent radicals remain intact for longer than 6 hours at RT and are directly characterized in the real space at the single-chemical-bond scale by means of BR-STM imaging. The chemical reactivity of radicals is investigated by model intermolecular radical transfer reactions. With the participation of as-synthesized phenyl radicals, the dehydrogenation reaction of Ext-TEBs takes place at around 200 K on Ag(111), in strong contrast to the finding that nondehydrogenated coupling of Ext-TEB takes place at 400 K on the same surface. Aided by the decoupling of radical generation and transfer processes, the reaction pathways can be accurately tuned by the rational choice of stoichiometric ratios of precursor molecules. Our studies not only provide strategies to prepare persistent radicals with high reactivity but also aid in clarifying the reaction pathways of radical reactions directly.

MATERIALS AND METHODS
STM measurements
All STM experiments were performed in an ultrahigh vacuum chamber (base pressure is better than 1×10^{-10} torr) equipped with a commercial low-temperature scanning tunneling microscope (Scienta Omicron). Single crystalline Ag(111) was cleaned by several cycles of argon ion sputtering and subsequent annealing. The ITP and Ext-TEB molecules were purchased from J&K Company (purity higher than 98%). ITP and Ext-TEB molecules were evaporated with a commercial Kentax TEC-BSC evaporator with evaporating rates of 0.06 and 0.02 ML/min, respectively. All STM measurements were carried out at 78 K with a tungsten tip, if not otherwise specifically stated. All BR-STM images were acquired in constant-height mode at 4.2 K with a CO-functionalized tungsten tip. All STM images were analyzed by WSxM software (62).

DFT methods
All DFT calculations were performed by the Vienna ab initio Simulation package together with an atomic simulation environment (63, 64). The electron-ion interactions were described by the projector augmented wave potentials (65), with the plane wave basis expanded to a kinetic energy cutoff of 400 eV. The exchange-correlation interactions were treated by the van der Waals density functional in the version of rev-vdWDF2 developed by Hamada (66, 67). Such a method has been demonstrated to be accurate for the adsorption of molecules on metal surfaces (68). The Ag(111) surface was represented by a four-layered slab using a $p(8 \times 10)$ supercell, and periodic image interactions were avoided by using a 15-Å vacuum layer. A 3 by 3 by 1 grid was used to sample the first Brillouin zone. The transition states were identified by using a combination of climbing image nudged elastic band (CI-NEB) and Dimer method (69, 70). First, 10 to 20 images were inserted between the initial and final states for each reaction and optimized by CI-NEB. The image with the highest energy was subsequently used as the input of the Dimer method to obtain the saddle point. All structures including local minima and saddle points were optimized until the residual force on each atom was lower than 0.02 eV/Å, except the bottom two layers of the Ag(111) surface, which were kept frozen.

Supplementary Materials
This PDF file includes:
Supplementary Text
Figs. S1 to S15
References

REFERENCES AND NOTES
1. X. Wang, A. Studer, Iodine(III) reagents in radical chemistry. *Acc. Chem. Res.* **50**, 1712–1724 (2017).

2. Y. Shen, C.-F. Chen, Helicenes: Synthesis and applications. *Chem. Rev.* **112**, 1463–1535 (2012).

3. R. Andrzej, Organic diradicals and polyradicals: From spin coupling to magnetism? *Chem. Rev.* **94**, 871–893 (1994).

4. D. Griller, K. U. Ingold, Persistent carbon-centered radicals. *Acc. Chem. Res.* **9**, 13–19 (1976).

5. W. He, H.-K. Kim, W. G. Wamer, D. Melka, J. H. Callahan, J.-J. Yin, Photogenerated charge carriers and reactive oxygen species in ZnO/Au hybrid nanostructures with enhanced photocatalytic and antibacterial activity. *J. Am. Chem. Soc.* **136**, 750–757 (2014).

6. D. Leifert, A. Studer, The persistent radical effect in organic synthesis. *Angew. Chem. Int. Ed. Engl.* **59**, 74–108 (2020).

7. L. Tebben, A. Studer, Nitroxides: Applications in synthesis and in polymer chemistry. *Angew. Chem. Int. Ed. Engl.* **50**, 5034–5068 (2011).

8. Z. X. Chen, Y. Li, F. Huang, Persistent and stable organic radicals: Design, synthesis, and applications. *Chem* **7**, 288–332 (2021).

9. D. G. de Oteyza, P. Gorman, Y.-C. Chen, S. Wickenburg, A. Riss, D. J. Mowbray, G. Etkin, Z. Pedramrazi, H.-Z. Tsai, A. Rubio, M. F. Crommie, F. R. Fischer, Direct imaging of covalent bond structure in single-molecule chemical reactions. *Science* **340**, 1434–1437 (2013).

10. Y. Zhao, K. Jiang, C. Li, Y. Liu, G. Zhu, E. Pizzochero, E. Kaxiras, D. Guan, Y. Li, H. Zheng, C. Liu, J. Jia, M. Qin, X. Zhuang, S. Wang, Quantum nanomagnets in on-surface metal-free porphyrin chains. *Nat. Chem.* **15**, 53–60 (2022).

11. E. Pérez-Elvira, A. Barragán, Q. Chen, D. Soler-Polo, A. Sánchez-Grande, D. J. Vicent, K. Lauwaet, J. Santos, P. Mutombo, J. I. Mendieta-Moreno, B. de la Torre, J. M. Gallego, R. Miranda, N. Martín, P. Jelínek, J. I. Urgel, D. Écija, Generating antiaromaticity in polycyclic conjugated hydrocarbons by thermally selective skeletal rearrangements at interfaces. *Nat. Synth.* **2**, 1159–1170 (2023).

12. T. Wang, H. Lv, Q. Fan, L. Feng, X. Wu, J. Zhu, Highly selective synthesis of cis-enediynes on a Ag(111) surface. *Angew. Chem. Int. Ed. Engl.* **56**, 4762–4766 (2017).

13. J. Li, N. Merino-Díez, E. Carbonell-Sanromà, M. Vilas-Varela, D. G. de Oteyza, D. Peña, M. Corso, J. I. Pascual, Survival of spin state in magnetic porphyrins contacted by graphene nanoribbons. *Sci. Adv.* **4**, eaaq0582 (2018).

14. S. Wang, P. Ding, Z. Li, C. Mattioli, E. Wenlong, Y. Sun, A. Gourdon, L. N. Kantorovich, F. Besenbacher, X. Yang, M. Yu, Subsurface-carbon-induced local charge of copper for an on-surface displacement reaction. *Angew. Chem. Int. Ed. Engl.* **60**, 23123–23127 (2021).

15. H. Zhou, J. Liu, S. Du, L. Zhang, G. Li, Y. Zhang, B. Z. Tang, H.-J. Gao, Direct visualization of surface-assisted two-dimensional diyne polycyclotrimerization. *J. Am. Chem. Soc.* **136**, 5567–5570 (2014).

16. J. Liu, J. Li, Z. Xu, X. Zhou, Q. Xue, T. Wu, M. Zhong, R. Li, R. Sun, Z. Shen, H. Tang, S. Gao, B. Wang, S. Hou, Y. Wang, On-surface preparation of coordinated lanthanide-transition-metal clusters. *Nat. Commun.* **12**, 1619 (2021).

17. A. Rastgoo-Lahrood, N. Martsinovich, M. Lischka, J. Eichhorn, P. Szabelski, D. Nieckarz, T. Strunskus, K. Das, M. Schmittel, W. M. Heckl, M. Lackinger, From Au-thiolate chains to thioether sierpiński triangles: The versatile surface chemistry of 1,3,5-tris(4-mercaptophenyl)benzene on Au(111). *ACS Nano* **10**, 10901–10911 (2016).

18. G. Zhan, Z.-F. Cai, K. Strutyński, L. Yu, N. Herrmann, M. Martínez-Abadía, M. Melle-Franco, A. Mateo-Alonso, S. Feyter, Observing polymerization in 2D dynamic covalent polymers. *Nature* **603**, 835–840 (2022).

19. M. Z. Hossain, H. S. Kato, M. Kawai, Fabrication of interconnected 1D molecular lines along and across the dimer rows on the Si(100)-(2 × 1)-h surface through the radical chain reaction. *Phys. Rev. B* **109**, 23129–23133 (2005).

20. Q. Fan, L. Yan, M. W. Tripp, O. Krejčí, S. Dimosthenous, S. R. Kachel, M. Chen, A. S. Foster, U. Koert, P. Liljeroth, J. M. Gottfried, Biphenylene network: A nonbenzenoid carbon allotrope. *Science* **372**, 852–856 (2021).

21. G. Galeotti, F. De Marchi, E. Hamzehpoor, O. MacLean, M. Rajeswara Rao, Y. Chen, L. V. Besteiro, M. Dettmann, L. Ferrari, F. Frezza, P. M. Sheverdyaeva, R. Liu, A. K. Kundu, P. Moras, M. Ebrahimi, M. C. Gallagher, F. Rosei, D. F. Perepichka, G. Contini, Synthesis of mesoscale ordered two-dimensional π-conjugated polymers with semiconducting properties. *Nat. Mater.* **19**, 874–880 (2020).

22. L. Lafferentz, V. Eberhardt, C. Dri, C. Africh, G. Comelli, F. Esch, S. Hecht, L. Grill, Controlling on-surface polymerization by hierarchical and substrate-directed growth. *Nat. Chem.* **4**, 215–220 (2012).

23. L. Schneider, P. Beck, J. Wiebe, R. Wiesendanger, Atomic-scale spin-polarization maps using functionalized superconducting probes. *Sci. Adv.* **7**, eabd7302 (2021).

24. M. Ziatdinov, O. Dyck, X. Li, B. G. Sumpter, S. Jesse, R. K. Vasudevan, S. V. Kalinin, Building and exploring libraries of atomic defects in graphene: Scanning transmission electron and scanning tunneling microscopy study. *Sci. Adv.* **5**, eaaw8989 (2019).

25. Z. Wang, R. Yin, J. Meng, J. Wang, Y. Liang, C. Ma, S. Tan, Q. Li, J. Yang, B. Wang, Self-limited embedding alternating 585-ringed divacancies and metal atoms into graphene nanoribbons. *J. Am. Chem. Soc.* **145**, 8445–8454 (2023).

26. C. S. Kley, J. Čechal, T. Kumagai, F. Schramm, M. Ruben, S. Stepanow, K. Kern, Highly adaptable two-dimensional metal-organic coordination networks on metal surfaces. *J. Am. Chem. Soc.* **134**, 6072–6075 (2012).

27. J. Su, M. Telychko, P. Hu, G. Macam, P. Mutombo, H. Zhang, Y. Bao, F. Cheng, Z.-Q. Huang, Z. Qiu, S. J. R. Tan, H. Lin, P. Jelínek, F.-C. Chuang, J. Wu, J. Lu, Atomically precise bottom-up synthesis of π-extended [5]triangulene. *Sci. Adv.* **5**, eaav7717 (2019).

28. L. Liu, H. Klaasen, M. C. Witteler, B. Schulze Lammers, A. Timmer, H. Kong, H. Mönig, H.-Y. Gao, J. Neugebauer, H. Fuchs, A. Studer, Polymerization of silanes through dehydrogenative Si-Si bond formation on metal surfaces. *Nat. Chem.* **13**, 350–357 (2021).

29. Q. Sun, X. Yu, M. Bao, M. Liu, J. Pan, Z. Zha, L. Cai, H. Ma, C. Yuan, X. Qiu, W. Xu, Direct formation of C-C triple-bonded structural motifs by on-surface dehalogenative homocouplings of tribromomethyl-substituted arenes. *Angew. Chem. Int. Ed. Engl.* **57**, 4035–4038 (2018).

30. P. H. Jacobse, Z. Jin, J. Jiang, S. Peurifoy, Z. Yue, Z. Wang, D. J. Rizzo, S. G. Louie, M. F. Crommie, M. Nuckolls, Pseudo-atomic orbital behavior in graphene nanoribbons with four-membered rings. *Sci. Adv.* **7**, eabl5892 (2021).

31. M. Ammon, T. Sander, S. Maier, On-surface synthesis of porous carbon nanoribbons from polymer chains. *J. Am. Chem. Soc.* **139**, 12976–12984 (2017).

32. N. Kalashnyk, K. Mouhat, J. Oh, J. Jung, Y. Xie, E. Salomon, T. Angot, F. Dumur, D. Gigmes, S. Clair, On-surface synthesis of aligned functional nanoribbons monitored by scanning tunnelling microscopy and vibrational spectroscopy. *Nat. Commun.* **8**, 14735 (2017).

33. P. Ruffieux, S. Wang, B. Yang, C. Sánchez-Sánchez, J. Liu, T. Dienel, L. Talirz, P. Shinde, C. A. Pignedoli, D. Passerone, T. Dumslaff, X. Feng, K. Müllen, R. Fasel, On-surface synthesis of graphene nanoribbons with zigzag edge topology. *Nature* **531**, 489–492 (2016).

34. J. Liu, B.-W. Li, Y.-Z. Tan, A. Giannakopoulos, C. Sanchez-Sanchez, D. Beljonne, P. Ruffieux, R. Fasel, X. Feng, K. Müllen, Toward cove-edged low band gap graphene nanoribbons. *J. Am. Chem. Soc.* **137**, 6097–6103 (2015).

35. W. Wang, X. Shi, S. Wang, M. A. Van Hove, N. Lin, Single-molecule resolution of an organometallic intermediate in a surface-supported Ullmann coupling reaction. *J. Am. Chem. Soc.* **133**, 13264–13267 (2011).

36. Q. Zhong, A. Ihle, S. Ahles, H. A. Wegner, A. Schirmeisen, D. Ebeling, Constructing covalent organic nanoarchitectures molecule by molecule via scanning probe manipulation. *Nat. Chem.* **13**, 1133–1139 (2021).

37. A. Kinikar, M. Di Giovannantonio, J. I. Urgel, K. Eimre, Z. Qiu, Y. Gu, E. Jin, A. Narita, X.-Y. Wang, K. Müllen, P. Ruffieux, C. A. Pignedoli, R. Fasel, On-surface polyarylene synthesis by cycloaromatization of isopropyl substituents. *Nat. Synth.* **1**, 289–296 (2022).

38. Y. He, M. Garnica, F. Bischoff, J. Ducke, M. L. Bocquet, M. Batzill, W. Auwärter, J. V. Barth, Fusing tetrapyrroles to graphene edges by surface-assisted covalent coupling. *Nat. Chem.* **9**, 33–38 (2017).

39. B. Schuler, S. Fatayer, F. Mohn, N. Moll, N. Pavliček, G. Meyer, D. Peña, L. Gross, Reversible bergman cyclization by atomic manipulation. *Nat. Chem.* **8**, 220–224 (2016).

40. M. Telychko, G. Li, P. Mutombo, D. Soler-Polo, X. Peng, J. Su, S. Song, M. J. Koh, M. Edmonds, P. Jelínek, J. Wu, J. Lu, Ultrahigh-yield on-surface synthesis and assembly of circumcoronene into a chiral electronic kagome-honeycomb lattice. *Sci. Adv.* **7**, eabf0269 (2021).

41. Z.-Y. Yi, Z.-C. Wang, R.-N. Li, Z.-H. Li, J.-J. Duan, X.-Q. Yang, Y.-Q. Wang, T. Chen, D. Wang, L.-J. Wan, Silver surface-assisted dehydrobrominative cross-coupling between identical aryl bromides. *J. Am. Chem. Soc.* **146**, 11342–11351 (2024).

42. D. Zhong, J.-H. Franke, S. K. Podiyanachari, T. Blömker, H. Zhang, G. Kehr, G. Erker, H. Fuchs, L. Chi, Linear alkane polymerization on a gold surface. *Science* **334**, 213–216 (2011).

43. D.-Y. Li, S.-W. Li, Y.-L. Xie, X. Hua, Y.-T. Long, A. Wang, P.-N. Liu, On-surface synthesis of planar dendrimers via divergent cross-coupling reaction. *Nat. Commun.* **10**, 2414 (2019).

44. S. Kawai, O. Krejčí, A. S. Foster, R. Pawlak, F. Xu, L. Peng, A. Orita, E. Meyer, Diacetylene linked anthracene oligomers synthesized by one-shot homocoupling of trimethylsilyl on Cu(111). *ACS Nano* **12**, 8791–8797 (2018).

45. S.-W. Hla, L. Bartels, G. Meyer, K.-H. Rieder, Inducing all steps of a chemical reaction with the scanning tunneling microscope tip: Towards single molecule engineering. *Phys. Rev. Lett.* **85**, 2777–2780 (2000).

46. K. Sun, O. J. Silveira, Y. Ma, Y. Hasegawa, M. Matsumoto, S. Kera, O. Krejčí, A. S. Foster, S. Kawai, On-surface synthesis of disilabenzene-bridged covalent organic frameworks. *Nat. Chem.* **15**, 136–142 (2023).

47. H. Kong, S. Yang, H. Gao, A. Timmer, J. P. Hill, O. Díaz Arado, H. Mönig, X. Huang, Q. Tang, Q. Ji, W. Liu, H. Fuchs, Substrate-mediated C-C and C-H coupling after dehalogenation. *J. Am. Chem. Soc.* **139**, 3669–3675 (2017).

48. S. Zint, D. Ebeling, T. Schlöder, S. Ahles, D. Mollenhauer, H. A. Wegner, A. Schirmeisen, Imaging successive intermediate states of the on-surface Ullmann reaction on Cu(111): Role of the metal coordination. *ACS Nano* **11**, 4183–4190 (2017).

49. J. Cai, P. Ruffieux, R. Jaafar, M. Bieri, T. Braun, S. Blankenburg, M. Muoth, A. P. Seitsonen, M. Saleh, X. Feng, K. Müllen, R. Fasel, Atomically precise bottom-up fabrication of graphene nanoribbons. *Nature* **466**, 470–473 (2010).

50. J. Wang, K. Niu, H. Zhu, C. Xu, C. Deng, W. Zhao, P. Huang, H. Lin, D. Li, J. Rosen, P. Liu, F. Allegretti, J. V. Barth, B. Yang, J. Björk, Q. Li, L. Chi, Universal inter-molecular radical transfer reactions on metal surfaces. *Nat. Commun.* **15**, 3030 (2024).

51. M. Bieri, M.-T. Nguyen, O. Gröning, J. Cai, M. Treier, K. Aït-Mansour, P. Ruffieux, C. A. Pignedoli, D. Passerone, M. Kastler, K. Müllen, R. Fasel, Two-dimensional polymer formation on surfaces: Insight into the roles of precursor mobility and reactivity. *J. Am. Chem. Soc.* **132**, 16669–16676 (2010).

52. X. Zhou, F. Bebensee, Q. Shen, R. Bebensee, F. Cheng, Y. He, H. Su, W. Chen, G. Q. Xu, F. Besenbacher, T. R. Linderoth, K. Wu, On-surface snthesis approach to preparing one-dimensional organometallic and poly-p-phenylene chains. *Mater. Chem. Front.* **1**, 119–127 (2017).

53. Y.-Q. Zhang, T. Paintner, R. Hellwig, F. Haag, F. Allegretti, P. Feulner, S. Klyatskaya, M. Ruben, A. P. Seitsonen, J. V. Barth, F. Klappenberger, Synthesizing highly regular single-layer alkynyl-silver networks at the micrometer scale via gas-mediated surface reaction. *J. Am. Chem. Soc.* **141**, 5087–5091 (2019).

54. J. Björk, Y.-Q. Zhang, F. Klappenberger, J. V. Barth, S. Stafström, Unraveling the mechanism of the covalent coupling between terminal alkynes on a noble metal. *J. Phys. Chem. C* **118**, 3181–3187 (2014).

55. Y.-Q. Zhang, N. Kepčija, M. Kleinschrodt, K. Diller, S. Fischer, A. C. Papageorgiou, F. Allegretti, J. Björk, S. Klyatskaya, F. Klappenberger, M. Ruben, J. V. Barth, Homo-coupling of terminal alkynes on a noble metal surface. *Nat. Commun.* **3**, 1286 (2012).

56. Y. Lyu, F. Gao, P. Cheng, L. Chen, S. Klyatskaya, M. Ruben, J. Rosen, J. V. Barth, J. Björk, K. Wu, Y.-Q. Zhang, Unraveling enyne bonding via dehydrogenation-hydrogenation processes in on-surface synthesis with terminal alkynes. *Adv. Mater. Interfaces* **11**, 202400222 (2024).

57. C. Zhang, R. B. Jaculbia, Y. Tanaka, E. Kazuma, H. Imada, N. Hayazawa, A. Muranaka, M. Uchiyama, Y. Kim, Chemical identification and bond control of π-skeletons in a coupling reaction. *J. Am. Chem. Soc.* **143**, 9461–9467 (2021).

58. A. Riss, A. P. Paz, S. Wickenburg, H. Z. Tsai, D. G. De Oteyza, A. J. Bradley, M. M. Ugeda, P. Gorman, H. S. Jung, M. F. Crommie, A. Rubio, F. R. Fischer, Imaging single-molecule reaction intermediates stabilized by surface dissipation and entropy. *Nat. Chem.* **8**, 678–683 (2016).

59. J. Lawrence, M. S. G. Mohammed, D. Rey, F. Aguilar-Galindo, A. Berdonces-Layunta, D. Peña, D. G. de Oteyza, Reassessing alkyne coupling reactions while studying the electronic properties of diverse pyrene linkages at surfaces. *ACS Nano* **15**, 4937–4946 (2021).

60. L. Xing, J. Li, Y. Bai, Y. Lin, L. Xiao, C. Li, D. Zhao, Y. Wang, Q. Chen, J. Liu, K. Wu, Surface-confined alternating copolymerization with molecular precision by stoichiometric control. *Nat. Commun.* **15**, 666 (2024).

61. C.-H. Shu, Y. He, R.-X. Zhang, J.-L. Chen, A. Wang, P.-N. Liu, Atomic-scale visualization of stepwise growth mechanism of metal-alkynyl networks on surfaces. *J. Am. Chem. Soc.* **142**, 16579–16586 (2020).

62. I. Horcas, R. Fernández, J. M. Gómez-Rodríguez, J. Colchero, J. Gómez-Herrero, A. M. Baro, WSXM: A software for scanning probe microscopy and a tool for nanotechnology. *Rev. Sci. Instrum.* **78**, 013705 (2007).

63. G. Kresse, J. Furthmüller, Efficient iterative schemes for *ab initio* total-energy calculations using a plane-wave basis set. *Phys. Rev. B Condens. Matter* **54**, 11169–11186 (1996).

64. A. Hjorth Larsen, J. Jørgen Mortensen, J. Blomqvist, I. E. Castelli, R. Christensen, M. Dułak, J. Friis, M. N. Groves, B. Hammer, C. Hargus, E. D. Hermes, P. C. Jennings, P. Bjerre Jensen, J. Kermode, J. R. Kitchin, E. Leonhard Kolsbjerg, J. Kubal, K. Kaasbjerg, S. Lysgaard, J. Bergmann Maronsson, T. Maxson, T. Olsen, L. Pastewka, A. Peterson, C. Rostgaard, J. Schiøtz, O. Schütt, M. Strange, K. S. Thygesen, T. Vegge, L. Vilhelmsen, M. Walter, Z. Zeng, K. W. Jacobsen, The atomic simulation environment—A python library for working with atoms. *J. Phys. Condens. Matter* **29**, 273002 (2017).

65. P. E. Blöchl, Projector augmented-wave method. *Phys. Rev. B* **50**, 17953–17979 (1994).

66. M. Dion, H. Rydberg, E. Schröder, D. C. Langreth, B. I. Lundqvist, Van der Waals density functional for general geometries. *Phys. Rev. Lett.* **92**, 246401 (2004).

67. I. Hamada, Van der Waals density functional made accurate. *Phys. Rev. B* **89**, 121103 (2014).

68. J. Björk, S. Stafström, Adsorption of large hydrocarbons on coinage metals: A van der Waals density functional study. *ChemPhysChem* **15**, 2851–2858 (2014).

69. G. Henkelman, B. P. Uberuaga, H. Jónsson, A climbing image nudged elastic band method for finding saddle points and minimum energy paths. *J. Chem. Phys.* **113**, 9901–9904 (2000).

70. G. Henkelman, H. Jónsson, A dimer method for finding saddle points on high dimensional potential surfaces using only first derivatives. *J. Chem. Phys.* **111**, 7010–7022 (1999).

71. J. Ren, M. Freitag, C. Schwermann, A. Bakker, S. Amirjalayer, A. Rühling, H. Y. Gao, N. L. Doltsinis, F. Glorius, H. Fuchs, A unidirectional surface-anchored n-heterocyclic carbene rotor. *Nano Lett.* **20**, 5922–5928 (2020).